CrossMark

X-Ray Emission from the Jets and Lobes of the Spiderweb

Christopher L. Carilli[1] , Craig S. Anderson[2] , Paolo Tozzi[3] , Maurilio Pannella[4], Tracy Clarke[5] , L. Pentericci[7] , Ang Liu[3],
Tony Mroczkowski[6,8] , G. K. Miley[9], H. J. Rottgering[9], S. Borgani[10,11,12,13] , Colin Norman[14,15] , A. Saro[10,11,12,13],
M. Nonino[10], and L. Di Mascolo[9]

[1] National Radio Astronomy Observatory, P.O. Box 0, Socorro, NM 87801, USA; ccarilli@nrao.edu
[2] Jansky Fellow of the National Radio Astronomy Observatory, P.O. Box 0, Socorro, NM 87801, USA
[3] INAF—Osservatorio Astrofisico di Arcetri, Largo E. Fermi 5, I-50127, Firenze, Italy
[4] Astronomy Unit, Department of Physics, University of Trieste, via Tiepolo 11, I-34131 Trieste, Italy
[5] Naval Research Laboratory, Code 7213, 4555 Overlook Ave. SW, Washington, DC 20375, USA
[6] Max Planck Institute for Extraterrestrial Physics, Giessenbachstrasse 1, D-85748 Garching, Germany
[7] INAF-OAR, Via Frascati 33, Monte Porzio Catone (RM), Italy
[8] European Southern Observatory, Karl-Schwarzschild-Str. 2, D-85748 Garching b. Munchen, Germany
[9] Leiden Observatory, Leiden University, P.O.Box 9513, NL-2300 RA, Leiden, The Netherlands
[10] Dipartimento di Fisica dell' Università di Trieste, Sezione di Astronomia, via Tiepolo 11, I-34131 Trieste, Italy
[11] INAF-Osservatorio Astronomico di Trieste, Via G.B. Tiepolo 11, I-34131 Trieste, Italy
[12] INFN, Sezione di Trieste, Via Valerio 2, I-34127 Trieste TS, Italy
[13] IFPU, Institute for Fundamental Physics of the Universe, via Beirut 2, I-34151 Trieste, Italy
[14] Space Telescope Science Institute, 3700 San Martin Dr., Baltimore, MD 21210, USA
[15] Johns Hopkins University, 3400 N. Charles Street, Baltimore, MD 212, USA
Received 2022 January 13; revised 2022 February 14; accepted 2022 February 14; published 2022 March 28

Abstract

Deep Chandra and Very Large Array imaging reveals a clear correlation between X-ray and radio emission on scales $\sim$100 kpc in the Spiderweb radio galaxy at $z = 2.16$. The X-ray emission associated with the extended radio source is likely dominated by inverse Compton upscattering of cosmic microwave background photons by the radio-emitting relativistic electrons. For regions dominated by high surface brightness emission, such as hot spots and jet knots, the implied magnetic fields are $\sim$50–70 μG. The nonthermal pressure in these brighter regions is then $\sim 9 \times 10^{-10}$ dynes cm^{-2}, or three times larger than the nonthermal pressure derived assuming minimum energy conditions, and an order of magnitude larger than the thermal pressure in the ambient cluster medium. Assuming ram pressure confinement implies an average advance speed for the radio source of $\sim$2400 km s^{-1} and a source age of $\sim 3 \times 10^7$ yr. Considering the lower surface brightness, diffuse radio-emitting regions, we identify an evacuated cavity in the Lyα emission coincident with the tail of the eastern radio lobe. Making reasonable assumptions for the radio spectrum, we find that the relativistic electrons and fields in the lobe are plausibly in pressure equilibrium with the thermal gas and close to a minimum energy configuration. The radio morphology suggests that the Spiderweb is a high-z example of the rare class of hybrid morphology radio sources (or HyMoRS), which we attribute to interaction with the asymmetric gaseous environment indicated by the Lyα emission.

Unified Astronomy Thesaurus concepts: Radio galaxies (1343); High-energy cosmic radiation (731); Radio jets (1347); Cosmic microwave background radiation (322)

1. Introduction

It is well documented that powerful radio active galactic nuclei (AGNs) act as beacons to massive galaxy formation in protoclusters in the early universe (Carilli et al. 2001; Miley & de Breuck 2008). The powerful radio-emitting jets are driven by mass accretion onto supermassive black holes and are thought to play a number of important roles in galaxy formation. Radio-mode feedback, meaning heating of the protocluster medium around the host galaxy by the radio jets on scales of tens to hundreds of kiloparsecs, is often invoked to suppress late-time gas accretion, thereby limiting high-mass galaxy growth (McNamara et al. 2005; Fabian 2012). Conversely, jet-induced star formation, induced by compression of dense gas in the host galaxies by shocks driven by the advancing radio source, may enhance star formation locally in some systems (Gaibler et al. 2012). The radio jets may also

remove angular momentum from the AGN accretion disk, thereby enhancing accretion rates and early SMBH formation (Blandford & Payne 1982). These same jets can also transport magnetic fields and possibly heavy elements to large scales in the protocluster (Carilli & Taylor 2002).

Among the best-studied powerful radio galaxies in a dense environment at large look-back time is the Spiderweb radio galaxy, J1140–2629, at $z = 2.16$ (Pentericci et al. 1997, 1999; Kurk et al. 2000; Miley et al. 2006; Miley & de Breuck 2008), with high-resolution imaging and spectroscopy at optical through radio wavelengths. The radio source is characterized by two jets oriented roughly east–west, extending about 7$''$ ($\sim$60 kpc) from the AGN. The protocluster shows a dense distribution of galaxies extending to radii >100 kpc, as well as an Lyα halo on a similar scale, with a major axis along the jet axis (Miley et al. 2006). Many of these galaxies have been detected in CO and thermal emission from warm dust, including the host galaxy of the radio source itself (Dannerbauer et al. 2014; Gullberg et al. 2016; Jin et al. 2021). There also appears to be a diffuse CO-emitting component on a $\sim$100 kpc scale (Emonts et al. 2016).
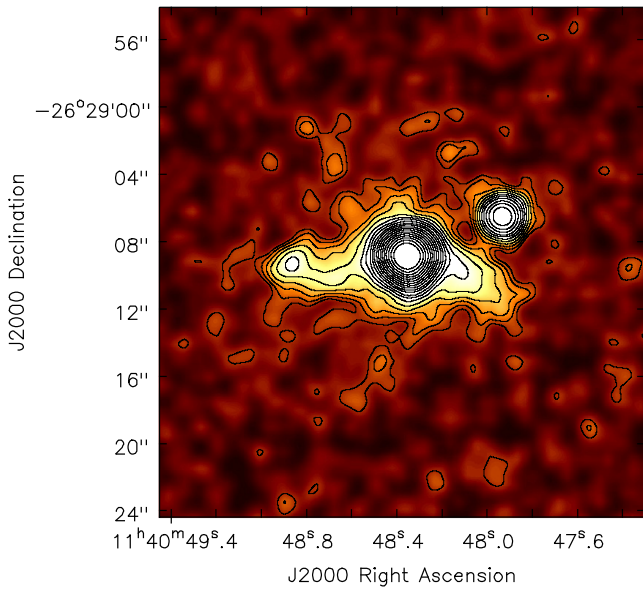
Figure 1. Contour and color scale image of the $z = 2.16$ powerful radio galaxy, J1140–2629 (the "Spiderweb galaxy"), from Chandra Observatory total X-ray emission (0.5–7 keV), convolved with a $1''$ Gaussian. This is the total counts image. Further processing, including AGN subtraction, will be presented in Tozzi et al. (2021). The contour levels are a geometric progression in the square root two, starting at 0.8 counts beam^{-1}.

A 28 ks (on-source) observation with Chandra revealed a dominant X-ray AGN, plus a faint extension of the X-ray emission along the radio jet (Carilli et al. 2002). However, a clean separation of the faint extended emission from the AGN was difficult with the limited exposure, and physical conclusions speculative. To date, a detailed understanding of the physical conditions (pressures, magnetic fields) in the radio source and the ambient medium in the Spiderweb complex remains limited.

We have embarked on a deep study of the Spiderweb galaxy using Chandra and the Jansky Very Large Array (VLA). We have obtained a 700 ks Chandra exposure, as well as broadband radio observations with arcsecond to subarcsecond resolution from 340 MHz to 36 GHz, and low spatial resolution observations with the ALMA Small Baseline Array (A. Saro et al. 2022, in preparation). In this paper, we present the extended X-ray emission associated with the radio jets and lobes on ~100 kpc scales. We derive magnetic fields and pressures in the source under the standard assumptions of inverse Compton (IC) upscattering of cosmic microwave background (CMB) photons by the relativistic synchrotron-emitting electrons in the outer regions of the source >20 kpc from the core. A future analysis will consider contributions of other photon fields over the full source (M. Sobolewska et al. 2022, in preparation). In parallel papers we explore the polarized radio emission and, in particular, study the magnetic field orientation in the radio source and the extreme rotation measures indicative of a magnetized ambient thermal gas (C. Anderson et al.2021, in preparation), the protocluster AGN population based on the deep X-ray exposure (Tozzi et al. 2021), and the nuclear X-ray source and diffuse emission away from the radio jets (P. Tozzi et al. 2021, in preparation).

2. Observations and Data Reduction

The Spiderweb galaxy was the target of a Chandra Large Program observation with ACIS-S (AO20; PI P. Tozzi). Data reduction is performed starting from the level-1 event files with CIAO 4.13, with the latest release of the Chandra Calibration Database at the time of writing (CALDB 4.9.3). The details of data reduction, including removal of spurious events and residual cosmic rays, and high-background filtering are described in Tozzi et al. (2021). The total effective exposure time is 715 ks.

We obtained deep VLA observations in 2019 September at X band (8–12 GHz) at $0''4 \times 0''2$ resolution (major axis oriented north–south, in all cases) and S band (2–4 GHz), at $1''3 \times 0''6$ resolution. We use "3 GHz" to designate the full S band and "10 GHz" to designate the full X band. A total of 8 hr was observed in each band.

Standard pipeline calibration was employed at the VLA,[16] using 3C 286 as the absolute flux density scale calibrator. The calibrated data were then threshold flagged and self-calibrated using both AIPS and CASA. The final imaging process employed the CLEAN algorithm, with Briggs weighting and a robust factor of zero (Briggs et al. 1999). Multiscale clean was employed, cleaning down to 2σ residuals. Bandwidth synthesis was also employed, across four 0.5 GHz bands spanning the 3 GHz band, and eight 1 GHz bands across the 8 GHz band. In each case, the images were restored with CLEAN Gaussian beams corresponding to the resolution at midband. The final images were summed to produce a single image for each band, while the subband images were also analyzed for spectral index across a given band. The resulting rms noise on the full-band images was 3 μJy beam^{-1} at 10 GHz and 5 μJy beam^{-1} at 3 GHz.

As part of the VLITE system (Clarke et al. 2016), commensal observations at 340 MHz (P band) with a resolution of $8''0 \times 4''3$ (major axis north–south) were obtained in parallel with our higher-frequency program. The VLITE 340 MHz data were processed using a dedicated flagging and calibration pipeline developed within the Obit (Cotton 2008) and AIPS (van Moorsel et al. 1996) data reduction packages. The pipeline uses automated flagging routines to remove radio frequency interference followed by standard delay, gain, and bandpass calibrations. The calibrated VLITE data were imaged using the wideband imaging algorithm MFimage in Obit to map a region of radius $1°$ from the pointing center with small facets. Two rounds of phase-only self-calibration were applied to the data. While all 4 days of observations were recorded with VLITE, the period of time in early 2019 September was known to be significantly impacted by ionospheric fluctuations; thus, we concentrate on the lowest noise day (rms noise 640 μJy beam^{-1}, 2019 September 13) for our analysis herein.

When comparing the Chandra X-ray and VLA radio images, we employ the standard astrometry for the Chandra observatory, as well as the astrometry set by the VLA calibrators, using J2000 coordinates. A check of the relative astrometry is given by the position of the active nucleus of the Spiderweb, for which we find agreement between the radio and X-ray to within $0''1$. The X-ray and radio alignments we consider herein are for structures on significantly large scales, ~$1''$ or greater. In particular, the quantitative spectra considered average over areas with a scale of a few arcseconds (see Figure 8).

---

[16] https://science.nrao.edu/facilities/vla/data-processing/pipeline
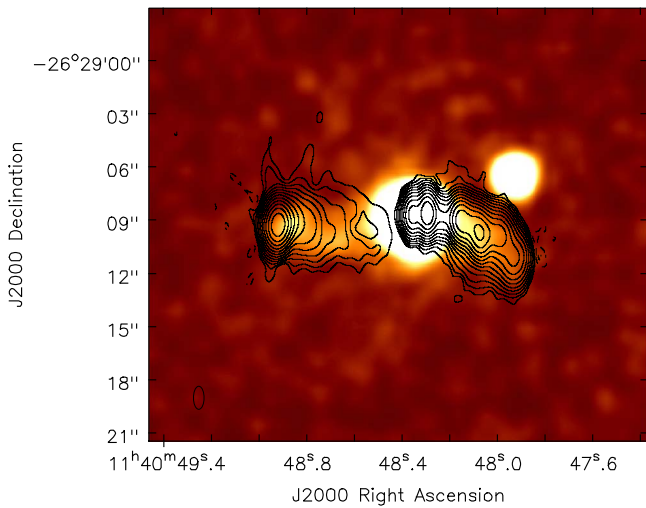
Figure 2. Contour image of the 2 GHz to 4 GHz VLA image of the Spiderweb galaxy, at a resolution of $1\rlap{.}{''}3 \times 0\rlap{.}{''}6$, major axis north–south. The contour levels are a geometric progression in a factor of two, starting at 20 μJy beam^{-1}. Negative contours are dashed. The color scale is the same Chandra Observatory total X-ray emission (0.5–7 keV) as shown in Figure 1.

We also employ an archival image of the Lyα emission from the Spiderweb. Narrowband imaging was carried out on 1999 April with ESO VLT Antu (UT1) using FORS1 in imaging mode (ESO program 63.O-0477(A), P.I. Miley; Kurk et al. 2000). The narrowband filter has a central wavelength of 381.4 nm and an FWHM of 6.5 nm. The diffuse emission in this filter is dominated by the rest-frame Lyα emission from the Spiderweb, although there remains some continuum emission in the filter as well. Details of these VLT observations and results will be presented in M. Nonino et al. (2022, in preparation). Here we present a morphological comparison of the Lyα and radio emission.

3. Results

3.1. Total Intensity Images

Figure 1 shows the total X-ray emission from 0.5 to 7 keV from the Chandra Observatory as both contour and color scale. The X-ray counts image has been convolved with a $1''$ Gaussian. The range 7–10 keV is not used for imaging since the signal is negligible and the background very high. However, the X-ray fluxes we derive refer to the range 0.5–10 keV (or separately 0.5–2 keV and 2–10 keV), since they are obtained from the full-band spectral analysis. Figure 2 shows the same X-ray image as color scale, with the VLA 3 GHz contour image at $1\rlap{.}{''}3 \times 0\rlap{.}{''}6$ resolution (major axis north–south).

The net count (background subtracted) for the full source in the 0.5–7 keV X-ray band is 10,400, which is dominated by emission from the AGN, which has $\sim$9600 counts. The net 0.5–7 keV X-ray counts for the western jet, outside of $2''$ radius from the core, is 200, while that for the eastern jet is 272. There is a point X-ray source $5''$ northwest of the AGN that appears to be associated with an optical galaxy in the protocluster at a large velocity offset from the main Spiderweb host galaxy. Likewise, there appears to be faint, diffuse emission north and south of the AGN, possibly indicating thermal emission from a hot ambient medium on scales of tens of kiloparsecs. We consider the AGN and other X-ray point sources, as well as thermal emission, in parallel papers (Tozzi et al. 2021; P. Tozzi
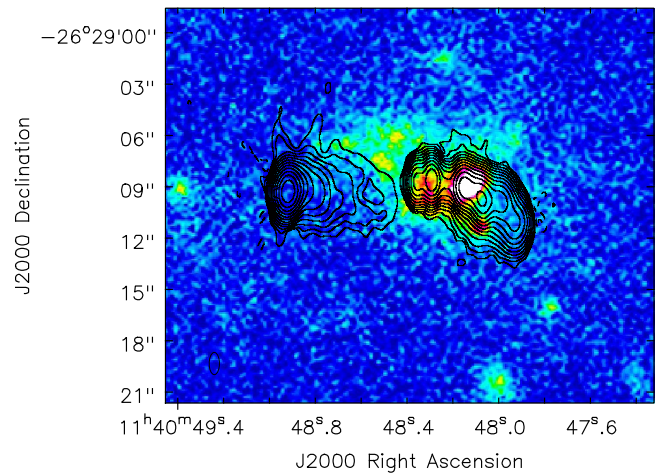
Figure 3. Same contour image as in Figure 1. The color image is the ESO narrowband filter image, roughly centered on the Lyα emission line from the Spiderweb galaxy at $z = 2.16$ (M. Nonino et al. 2022, in preparation).

et al. 2021, in preparation). The focus of this paper is the extended X-ray emission associated with the radio jets.

The rms noise on the 3 GHz image is 5.5 μJy beam^{-1}. The radio emission to the west shows a prominent jet, defined by a series of hot spots and more diffuse emission, extending at least $7''$ ($\sim$60 kpc), from the AGN, and becoming fainter with distance from the AGN. The emission to the east shows a bright radio hot spot at the source extremity, about $7''$ from the AGN, and fainter emission from a radio lobe between this hot spot and the AGN. The width of the eastern radio lobe, as well as the more diffuse regions of the western jet, is about $3''$ ($\sim$25 kpc), down to the 5σ level.

The extended X-ray emission follows closely the radio jets to both the east and west. There is an X-ray hot spot toward the end of the eastern lobe, close to, but not exactly aligned with, the radio hot spot, with an offset of $\sim$0$\rlap{.}{''}7$. Again, we estimate that the relative X-ray and radio astrometry is accurate to $\sim$0$\rlap{.}{''}1$, based on the strong AGN emission at both wave bands. We consider this X-ray–radio hot spot offset in M. Sobolewska et al. (2022, in preparation).

Figure 3 shows the 3 GHz radio contours and the ESO Lyα image (M. Nonino et al. 2022, in preparation). Extended Lyα emission is seen from the Spiderweb, which, at lower surface brightness, extends over more than 100 kpc, enveloping the protocluster (Miley & de Breuck 2008). Here we focus on the brighter Lyα emission regions toward the center of the protocluster. Note that the Lyα emission does not peak at the location of the AGN, likely the result of dust obscuration toward the galaxy center. In general, obscuration will be an issue when interpreting UV measurements.

There are two features of note with the comparison of the Lyα with the radio jets. First, on the western side, the radio jet deflects to the southwest just at a position of the brightest Lyα knot. This spatial coincidence suggests a physical association of the ambient thermal gas and the material within the radio jet, such as a strong shock where the fluids collide. This region will be discussed at length in a future paper, including the polarized radio emission (C. Anderson et al. 2021, in preparation).

The second Lyα–radio (anti)association is in the tail of the eastern lobe. There is a clear deficit of Lyα emission at the position of the diffuse radio lobe, and the Lyα emission follows the inner edge of the radio lobe. Again, this anticoincidence
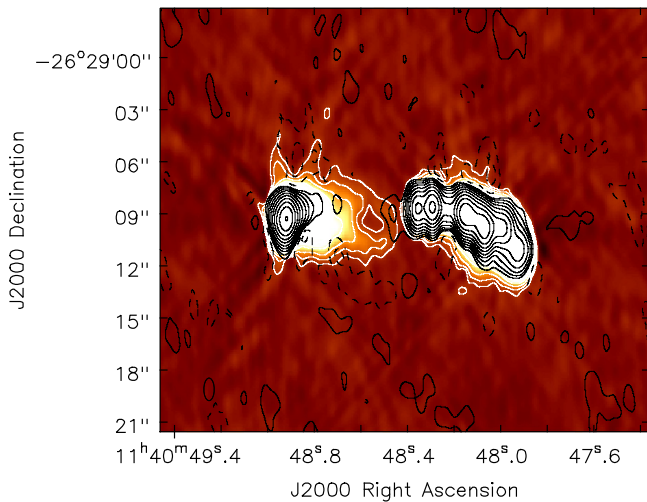
Figure 4. The color scale is the 2–4 GHz VLA image of the Spiderweb galaxy, as shown in Figure 1, saturated in intensity to show the low surface brightness emission. The white contours are the same as in Figure 1 for the 2–4 GHz image. The black contours are the 8–12 GHz integrated emission, convolved to the same resolution as the S-band image ($1\rlap{.}''3 \times 0\rlap{.}''6$). The contour levels are a geometric progression in factor of two, starting at $20\,\mu$Jy beam^{-1}.

Figure 5. Integrated radio spectrum of the Spiderweb radio galaxy.

Figure 6. The color scale is the spectral index across the 2–4 GHz band, at the same resolution as shown in Figure 1, blanked at 8σ. The contours are the same as in Figure 1.

suggests a physical association, in which the radio lobe somehow excludes the thermal gas, such as has been seen, for example, for radio cavities in lower-redshift X-ray clusters (McNamara et al. 2005).

Figure 4 shows the 10 GHz radio emission as black contours, plus a saturated color scale image of the 3 GHz radio emission, with the lower 3 GHz contours in white. The 10 GHz image has been convolved with the same Gaussian restoring beam as the 3 GHz image and has an rms noise of $5\,\mu$Jy beam^{-1}. This image shows the close association of the brighter radio knots all along the western jet and for the eastern radio hot spot. However, the eastern radio lobe is undetected at 10 GHz down to very low surface brightness levels, implying a very steep radio spectrum, $\alpha < -2.5$.
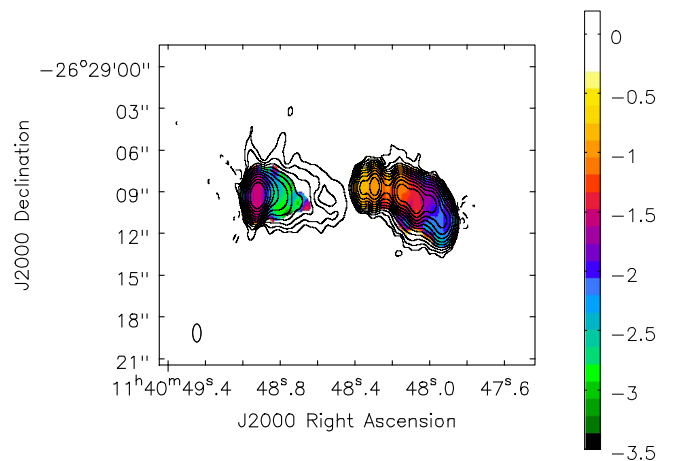
3.2. Spectra and Spectral Index

Figure 5 shows the integrated radio spectrum of the Spiderweb from 150 MHz to 36 GHz. The data are roughly consistent with a single power-law index of $\alpha = -1.3 \pm 0.1$, across the full frequency range, where spectral index is defined as $S_\nu \propto \nu^\alpha$. There is evidence for modest steepening at high frequency, with the spectral index changing from -1.15 ± 0.15 between 150 and 1450 MHz to -1.4 ± 0.1 between 3 and 32 GHz. The integrated spectrum mixes emission components across the source, including the core, flatter-spectrum knots, and steep-spectrum lobes, and hence is of limited use for extrapolation of spectral properties in particular regions.

Figure 6 shows the spectral index between images at 2.2 and 3.8 GHz, along with the 3 GHz total intensity image. The radio core and first western jet knot have spectral indices $\leqslant -1$, while the brighter knots further along the western jet and the radio hot spot at the end of the eastern lobe have steeper spectral indices $\sim -1.3 \pm 0.2$. The outer jet to the west shows spectral steepening to $\alpha < -2$ with distance from the core, while the diffuse tail of the eastern lobe is very steep spectrum, with $\alpha \leqslant -2.5$ in regions where it could be measured. For comparison, the spectral index study in Pentericci et al. (1997) shows steeper spectra in most regions between 4 and
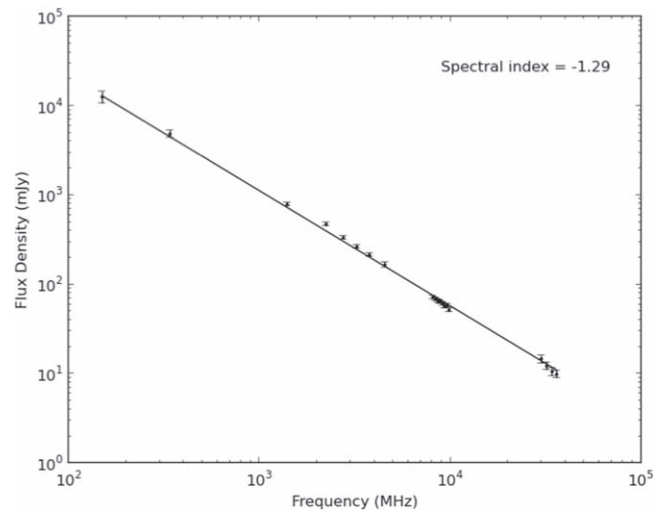
8 GHz, indicative of significant curvature (steepening), above 3 GHz.

Figure 7 shows the spectral index between 3 and 340 GHz at lower spatial resolution. In this case, the resolution is adequate to only get two independent measurements: one for the western jet, and one for the eastern hot spot plus radio lobe. Both are consistent with the integrated spectral index for the full source of -1.3 ± 0.1.
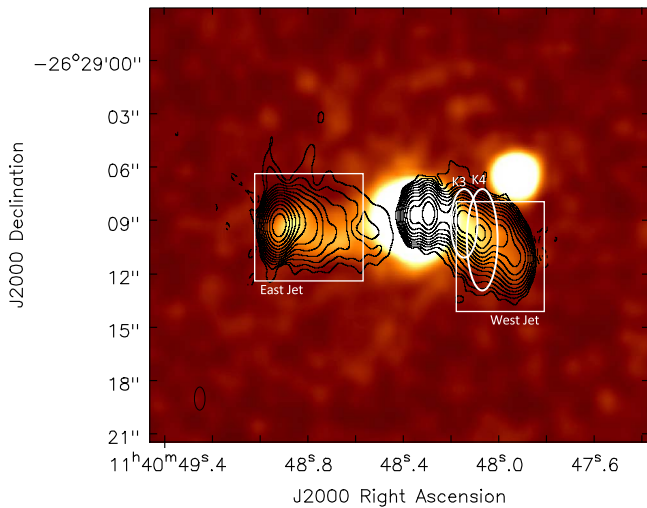
4. Analysis

4.1. Regions and Flux Densities

Figure 8 shows the regions chosen for analysis. These regions were chosen to avoid emission from the bright AGN (radii $>2\rlap{.}''5$ from the AGN), while capturing the outer eastern and western radio jet emission. We discuss the choice of regions in more depth below. Table 1 lists the 340 MHz and 3 GHz radio flux densities for the regions in Columns (2) and (3). Column (4) lists the spectral indices. For the larger regions, the spectral index is between 340 MHz and 3 GHz. For the smaller regions (K3 and K4), the spectral index is between 2 and 4 GHz. The errors include off-source rms noise plus gain uncertainties estimated during the flux bootstrap calibration
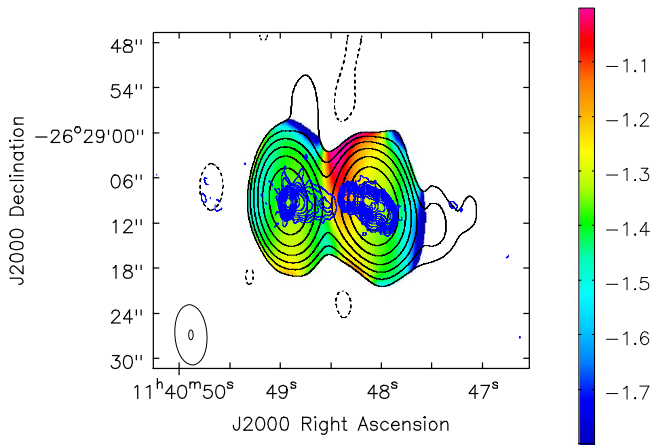
Figure 7. The color scale is the spectral index between 340 MHz and 3 GHz, at the resolution of the 340 MHz image ($8.''0 \times 4.''3$, major axis north–south). The black contours are the surface brightness at 340 MHz with geometric contour levels in factor of two, starting at 20 mJy beam^{-1}. The blue contours are the same as in Figure 1.

Figure 8. Same X-ray total counts color image and 3 GHz contours, with boxes and ellipses indicating the four regions for the IC and synchrotron analysis in Section 4.2.

process. For the west jet at 340 MHz, we subtracted the contribution of the AGN itself and the innermost west jet knot, since these contribute to the low-resolution 340 MHz flux density but are outside the region used for the X-ray summation. The contributions (about 10%) were estimated by extrapolating from 3 GHz using the measure spectral indices ~ -1.2 of these features (see Figure 6).

For the X-ray analysis of the jet emission, we have subtracted the background, and we have subtracted any residual contribution from the bright, compact AGN emission due to the far-out wings of the Chandra point-spread function. We have also subtracted possible diffuse thermal emission (P. Tozzi et al. 2021, in preparation). These components contribute $\sim 25\%$ to the measured totals in the regions. The jet X-ray fluxes (in erg cm^{-2} s^{-1}) in the soft band (0.5–2.0 keV) and hard band (2.0–10 keV) for the regions are listed in Columns (5) and (6). Also listed are the power-law indices for the X-ray emission, derived from fitting power-law spectra jointly across the soft and hard X-ray bands (Column (7)). The X-ray spectral index in frequency, α, relates to the X-ray photon index as

$\alpha = 1.0$ - photon index. The X-ray flux errors are based on photon statistics, while the errors for the spectral indices are derived during the fitting process. For the magnetic field and pressure analysis below, the dominant uncertainties arise from the assumptions in the model calculations, and we quote the model uncertainties explicitly where relevant.

The X-ray frequency relates to photon energy, $E_{\rm keV}$, as $\nu_x = 2.44 \times 10^{17} \times E_{\rm keV}$ Hz. We adopt an effective frequency, ν_x, equal to the geometric mean of the low- and high-energy limits of a given Chandra band (appropriate for a power-law spectrum of index ~ -1, consistent with the X-ray measurements). The corresponding values for the soft and hard bands are 2.44×10^{17} Hz and 1.11×10^{18} Hz, respectively.

To derive X-ray flux densities required for the IC calculation below (in Jy $= 10^{-23}$ erg s^{-1} cm^{-2} Hz^{-1}), we adopt a spectral index of $\alpha \sim -1.0$, for which the flux density becomes $S_\nu = S_{\rm band}/(\nu_x \times \ln(\nu_{\rm high}/\nu_{\rm low}))$, where $S_{\rm band}$ is the measured band-integrated flux (in erg cm^{-2} s^{-1}) and $\nu_{\rm high}$, $\nu_{\rm low}$ are the high and low frequencies of the band. Again, ν_x is the geometric mean between $\nu_{\rm high}$ and $\nu_{\rm low}$. This equation is accurate to $\sim 15\%$ for $\alpha = -1.0 \pm 0.2$. The X-ray flux densities at the effective frequencies for the soft and hard Chandra bands are given in Columns (8) and (9) in Table 1. We include the 15% uncertainty in flux density due to spectral index uncertainty in the table.

4.2. X-Ray Mechanisms

The very close association between X-ray and radio emission along both the eastern and western jets in the Spiderweb suggests physically related emission mechanisms. One possible mechanism to explain this spatial coincidence is X-ray synchrotron radiation from an extrapolation of the radio-emitting relativistic electron population to very high energy. However, even if we assume no spectral steepening between radio and X-ray frequencies, extrapolating the radio flux densities into the X-ray underpredicts the observed X-ray flux densities by a factor of ~ 40. Hence, the observed X-rays are much too bright to be an extrapolation of the radio synchrotron spectra to very high energy.

A second mechanism to explain the relationship could be thermal emission from shocked gas surrounding the expanding radio source. This mechanism was favored by Carilli et al. (2002) based on shorter Chandra observations, where the extended X-ray emission was detected at low significance and difficult to separate from the AGN itself. The deep X-ray image presented herein implies a substantially lower X-ray flux for the emission along the jet (the difference arising from a poor subtraction of the AGN in the Carilli et al. 2002 analysis). The new observations show that the X-ray emission is immediately coincident with the radio jets and not along the edges of the radio source—the latter being expected for thermal X-ray emission from a shocked cocoon (Snios et al. 2018).

Based on the morphology, flux, and spectral index (see Section 4.3), we posit that the most physically plausible mechanism to explain the radio−X-ray association along the jet is IC upscattering of the ambient photon field by the synchrotron-emitting relativistic electrons. This mechanism has long been considered in the context of X-ray emission from cosmic radio sources (Harris & Grindlay 1979), and it has been pointed out that upscattering of the CMB photons could become a dominant X-ray emission mechanism in high-redshift sources, due to the strong increase in the CMB energy density

Table 1
Observed Properties

Region	$S_{340\ \mathrm{MHz}}$ (Jy)	$S_{3\ \mathrm{GHz}}$ (mJy)	$\alpha_{0.34}^{3}$ or α_{2}^{4}	S_{soft} (10^{-15} erg cm^{-2} s^{-1})	S_{hard} (10^{-15} erg cm^{-2} s^{-1})	$\alpha_{\mathrm{soft}}^{\mathrm{hard}}$	$S_{2.4e17Hz}$ (10^{-11} Jy)	$S_{1.1e18Hz}$ (10^{-11} Jy)	Area (arcsec^2)
West jet	2.6 ± 0.4	170 ± 12	-1.2 ± 0.1	1.2 ± 0.13	1.4 ± 0.14	-1.0 ± 0.2	35 ± 6	7.9 ± 1.4	27
East jet	1.8 ± 0.3	111 ± 8	-1.3 ± 0.1	1.5 ± 0.14	1.1 ± 0.12	-1.3 ± 0.2	46 ± 8	6.4 ± 1.1	30
K3	$\cdots$	51 ± 4	-1.2 ± 0.2	0.22 ± 0.05	0.16 ± 0.04	-1.3 ± 0.2	6.5 ± 1.8	0.92 ± 0.24	2.4
K4	$\cdots$	86 ± 6	-1.4 ± 0.2	0.33 ± 0.6	0.41 ± 0.8	-1.0 ± 0.2	9.8 ± 2.4	2.3 ± 0.6	5.1

Table 2
Magnetic Fields and Energy Densities

Region	$B_{\mathrm{IC,soft}}$ (μG)	$U_{\mathrm{BIC,soft}}$ (erg cm^{-3})	$B_{\mathrm{IC,hard}}$ (μG)	$U_{\mathrm{BIC,hard}}$ (erg cm^{-3})	B_{minE} (μG)	U_{minE} (erg cm^{-3})
West jet	60	1.4×10^{-10}	54	1.2×10^{-10}	103	9.9×10^{-10}
East jet	45	8.1×10^{-11}	50	1.0×10^{-10}	95	8.4×10^{-10}
West jet K3	68	1.8×10^{-10}	76	2.3×10^{-10}	125	1.4×10^{-9}
West jet K4	72	2.0×10^{-10}	63	1.6×10^{-10}	125	1.4×10^{-9}

with redshift (Tavecchio et al. 2000; Schwartz 2002; Hodges-Kluck et al. 2021). Numerous studies have now shown that resolved X-ray emission from high-redshift radio jets is best interpreted as IC emission (Scharf et al. 2003; Cheung et al. 2012; Marshall et al. 2018; Ighina & Caccianiga 2019; Worrall et al. 2020; Hodges-Kluck et al. 2021; Snios et al. 2021), and even in some sources without extended radio emission (Simionescu et al. 2016; Schwartz et al. 2019).

4.3. Magnetic Fields Derived from CMB IC Emission

X-ray IC emission and the radio synchrotron emission arise from the same power-law distribution of relativistic electrons: the X-rays correspond to upscattering of the ambient photon field, and the radio emission is, in a quantum mechanical sense, upscattering of the virtual photons that compose the static magnetic field. Hence, if one knows the energy density of the ambient photon field, then the X-ray emission effectively "counts" the relativistic electrons, which, using the radio luminosity, then dictates the magnetic field strength (Longair 2011).

An important consistency check is agreement between the X-ray and radio spectral indices, given that the emission arises from the same power-law distribution of electrons. For all the regions analyzed herein, the spectral indices in the radio and X-ray agree, within the errors, with a value of -1.2 ± 0.2.

Considering the ambient photon field, for high-z radio galaxies it has been shown that the ambient photons relevant for comparison of the observed radio synchrotron and X-ray IC emission are in the submillimeter through far-IR (FIR; Scharf et al. 2003; Simionescu et al. 2016; Schwartz et al. 2019). While the Spiderweb is known to be luminous in the FIR (Seymour et al. 2012), the dominant FIR emission is isolated to the inner $\leqslant 1''$ radius (Gullberg et al. 2016). Gullberg et al. (2016) estimate an FIR luminosity of the host galaxy of $4.4 \times 10^{12}\ L_{\odot}$. For a centrally concentrated emitting region, the photon density behaves as $3L/(4\pi r^2 c)$, where L is the luminosity and r the radius (e.g., Scharf et al. 2003). The CMB energy density behaves as $U_{\mathrm{CMB}} = 4.2 \times 10^{-13} \times (1 + z)^4$ erg cm^{-3}. Comparing the CMB to the centrally sourced FIR, one finds that the CMB dominates the energy density beyond ~ 20 kpc, or $2''.4$, from the nucleus. Note that our high-resolution images imply that the

synchrotron photon energy density is below the CMB, even in the higher surface brightness regions.

For the preliminary analysis presented herein, we will focus on the outer regions of the source (radii >20 kpc from the core) and adopt the CMB as the ambient photon field. A more complete treatment of the full extent of the source, including spectral contributions from various photon fields, will be given in M. Sobolewska et al. (2022, in preparation).

The magnetic field calculation assuming upscattering of the CMB was first presented by Harris & Grindlay (1979) and is given by

$$B_G^{(1-\alpha)} = 5.75 \quad \times \quad 10^{-17} \times (5.05 \times 10^4)^{-\alpha} \\ \times (1 + z)^{(3-\alpha)} \times [S_r \times \nu_r^{-\alpha} / S_x \times \nu_x^{-\alpha}],$$

where S_x and S_r are the X-ray and radio flux densities at observed frequencies, ν_x and ν_r (all in matching units), and spectral index is defined as $S = \nu^{\alpha}$. Again, α is dictated by the power-law relativistic electron energy distribution and should be common to both the X-ray and radio emission.

We examine four regions for which adoption of a spectral index of -1.2 ± 0.2 in the X-ray and radio is reasonable. The regions are delineated in Figure 8. Two large regions capture the integrated X-ray emission and radio emission at 340 MHz, for the east and west jets beyond $\sim 2''.5$ from the AGN, respectively. These larger regions average over the source structure east and west of the nucleus in large boxes that contain all the emission; hence, the results are weighted toward the brighter radio hot spots and jet knots. We also consider spatially resolved measurements at 3 GHz of the two brightest knots beyond $2''.5$ from the AGN, for which the spectral index between 2 and 4 GHz is consistent with $\alpha = -1.2 \pm 0.2$.

Table 1 lists the X-ray and radio flux densities for the four regions. Using the Harris & Grindlay (1979) equation then leads to the magnetic fields listed in Table 2. For the larger regions, we derive IC magnetic field strengths of $\sim 50\ \mu$G. The implied magnetic energy density ($B^2/8\pi$ erg cm^{-3}, for B in G) is $\sim 1.0 \times 10^{-10}$ erg cm^{-3}. For the two bright western jet knots, we obtain field values $\sim 70\ \mu$G, and correspondingly a factor of two higher magnetic energy densities. The field values derived from the soft and hard bands are consistent to within 20%. An uncertainty in the spectral index of 0.2 implies an uncertainty in the magnetic field of $\sim 20\%$.

4.4. Minimum Energy Radio Synchrotron Calculations

Assuming a minimum energy configuration of relativistic particles and magnetic fields to estimate energy densities and magnetic fields in celestial synchrotron sources was first presented by Burbidge (1956). We adopt Equations (1) and (2) in Miley (1980). Note that assuming energy equipartition between fields and relativistic particles, as opposed to a minimum energy configuration, leads to field values 8% higher and a total energy density within 1% of the minimum (Carilli 1989; Readhead 2021).

We assume the standard values of electron/proton energy density = 1, filling factor = 1, a low frequency cutoff of 10 MHz, and a high frequency cutoff of 32 GHz (Miley 1980). The calculation is relatively insensitive to the frequency cutoffs: raising the low frequency cutoff by a factor of five increases the fields derived from the minimum energy assumption by 30%, and the high frequency cutoff has an even smaller effect.

We have adopted a low-frequency spectral index of $\alpha = -1.2$. Changing α by ± 0.2 alters the derived fields by about 25%, with steeper α leading to higher fields. In all cases, we assume a line-of-sight path length of 25 kpc ($\sim 3''$), corresponding to the width of the eastern lobe and western jet down to the 5σ surface brightness level.

The field values and minimum energy densities are listed in Table 2. The values derived are comparable to the early analysis in Pentericci et al. (1997). The typical field values derived assuming minimum energy are about a factor of two higher than those derived from the IC calculation. The implied minimum energy densities (summed fields and relativistic particles) are then about eight times higher than the magnetic energy density derived from the IC calculation. This factor of eight arises from the fact that the minimum energy fields are $\sim 2\times$ higher, meaning a factor of four higher magnetic energy density, and then there is another factor of two when including the relativistic particles.

4.5. Pressures

The minimum energy calculation for the synchrotron emission assumes that a minimum energy configuration is established by the relativistic particles and magnetic fields, implying equipartition of energy between fields and particles. There is no a priori reason to assume that such a minimum energy configuration is established. Hence, in the following analysis, we adopt the IC fields and consider the implications for pressures within the radio source, in comparison to the ambient medium. The relevant quantity is the total nonthermal pressure, meaning the summed pressure in fields and relativistic particles. Hence, the synchrotron radio emission provides a critical constraint, since it must be explained in the context of the IC derived magnetic field strength, and hence dictates the total nonthermal pressure.

The synchrotron minimum energy density implies a minimum pressure, which, for an isotropic relativistic gas, equals $1/3 \times$ energy density. Hence, the implied minimum pressure based on the synchrotron emissivity is $\sim 3 \times 10^{-10}$ dynes cm^{-2} (Table 2). However, the IC magnetic field strengths are a factor of two lower than dictated by the minimum energy assumption. For fields lower than the minimum configuration, the total nonthermal energy density (and pressure) increases as $(B/B_{\mathrm{minE}})^{3/2}$, in order to generate the observed radio emissivity. In this case, the pressure is dominated by the relativistic particles. For reference, for fields larger than B_{minE}, the total nonthermal pressure increases as $(B/B_{\mathrm{minE}})^{2}$, as the total pressure becomes dominated by the field (Readhead 2021; Carilli 1989). A field strength a factor of two lower than minimum energy then implies a factor of ~ 3 higher total nonthermal pressure $\sim 9 \times 10^{-10}$ dynes cm^{-2}.

The first conclusions based on the X-ray and radio emission from the jets of the Spiderweb are that the nonthermal pressures within the radio source are larger than dictated by minimum energy by a factor of three and are dominated by relativistic particles, not magnetic fields.

The Lyα emission provides a rough estimate of the thermal gas pressures in the Spiderweb protocluster. Pentericci et al. (1997) derive a typical density for the Lyα-emitting knots in the Spiderweb of ~ 40 cm^{-3}. Assuming a temperature of $\sim 10^{4}$ K implies a thermal pressure of 5.5×10^{-11} dynes cm^{-2}.

An important point to keep in mind is that the volume filling factor for the dense Lyα-emitting gas is small ($\sim 10^{-5}$; McCarthy 1993; Pentericci et al. 1999). Hence, there must be a hot, intercloud medium confining the line-emitting clouds. P. Tozzi et al. (2021, in preparation) have nominally identified X-ray emission from this hot, diffuse medium in the Spiderweb, on the same spatial scale as the Lyα and radio jet emission, by subtracting the strong X-ray AGN, and by avoiding regions that may be contaminated by the X-ray jets. They estimate an average gas density and temperature in a sphere of radius 50 kpc of $n_e \sim 0.014 \pm 0.0014$ cm^{-3} and $T \sim 2.4^{+0.5}_{-0.8} \times 10^{7}$ K. The implied thermal pressure is then $(4.6 \pm 1.3) \times 10^{-11}$ dynes cm^{-2}. Encouragingly, this hot gas pressure is comparable to the pressure derived from the Lyα emission, and both imply an ambient thermal gas pressure an order of magnitude lower than the nonthermal pressures derived above for the bright radio-emitting regions. A more detailed analysis of the cluster density radial profile is currently in progress.

The second conclusion therefore is that the high surface brightness radio-emitting regions (hot spots and jet knots) are overpressured relative to the ambient thermal gas in the cluster, by more than an order of magnitude.

Assuming ram pressure confinement of the radio structures then implies a typical advance speed for the radio source $v_{\mathrm{ram}} = (P_{\mathrm{nt}}/\rho)^{1/2} \sim 2400$ km s^{-1}, where ρ is the ambient mass density. Using the source maximum radius ~ 60 kpc implies a source age of $\sim 3 \times 10^{7}$ yr.

4.6. The Tail of the Eastern Lobe

We reemphasize that the calculations for the regions above are weighted to the higher brightness regions of the source, such as hot spots and jet knots, and hence to regions of higher pressure. As a final calculation, we consider the synchrotron minimum energy density in the very low surface brightness, steep-spectrum tail of the eastern radio lobe (but still beyond 20 kpc from the core). This is the region that shows the "cavity" in the Lyα emission coincident with the radio lobe.

The difficulty in calculating the pressure in the diffuse radio lobe is, again, that spatially resolving observations are only available at 3 GHz, and that the spectrum at this high frequency is seen to be very steep, ~ -2.5, but must flatten to lower frequency to explain the integrated radio spectrum of the source. In this case, we use the typical surface brightness in the tail of the radio lobe of $\sim 50 \, \mu$Jy beam^{-1} at 3 GHz, where the

beam is $1''.3 \times 0''.6$. We extrapolate the 3 GHz surface brightness to 1 GHz using the steep spectral index, implying a surface brightness at 1 GHz of $\sim 780\ \mu$Jy beam^{-1}. We then calculate the synchrotron minimum energy density using this 1 GHz surface brightness and the lower-frequency spectral index, $\alpha = -1.2$, as above. This calculation leads to a magnetic field strength of 37 μG, a minimum nonthermal energy density of 1.3×10^{-10} erg cm^{-3}, and a minimum nonthermal pressure of 4×10^{-11} dynes cm^{-2}. Decreasing the turnover frequency from 1 to 0.5 GHz increases the minimum nonthermal pressure by 60%.

Hence, if the diffuse tails of the radio lobes have a spectral flattening between 0.5 and 1 GHz, and if the fields and particles have been able to reach a minimum energy configuration in these potentially more relaxed and older regions, then the nonthermal radio lobe pressure is comparable to the thermal pressures of the ambient medium.

5. Discussion

We comment on one curiosity and a general question. Considering the radio source morphology, the eastern jet of the Spiderweb shows a radio hot spot at the extremity of the lobe, with clear spectral steepening from the hot spot back toward the AGN. Conversely, the western jet shows a gradual decline in surface brightness and spectral steepening with distance from the AGN. The eastern morphology, in both intensity and spectrum, is characteristic of high-power radio Fanaroff-Riley Class II radio galaxies ("edge-brightened," typically with $P_{178\mathrm{MHz}} > 10^{35}$ erg s^{-1} Hz^{-1}), while the western jet is typical of lower-power FR I ("edge-darkened") radio jets (Fanaroff & Riley 1974). However, the Spiderweb is one of the most luminous radio galaxies known, with $P_{178\mathrm{MHz}} \sim 4.6 \times 10^{36}$ erg s^{-1} Hz^{-1}, placing it several orders of magnitude above the canonical FR II/FR I break. Why then the dichotomy in both morphology and spectral index between lobes?

The Spiderweb is a high-redshift example of a hybrid morphology radio source (or HyMoRS), which is a known but rare and poorly understood class of radio galaxy, first described by Gopal-Krishna (2000), and for which correlated differences in morphology and spectral index between lobes have previously been observed (Gawronski et al. 2006; de Gasperin 2017). Their nature is not well constrained: they may arise because of the physical attributes of the source (e.g., jet power) or its environment (Kapinska et al. 2017), or because of observational or orientation effects (Harwood et al. 2020), or by some combination of these.

In the case of the Spiderweb system, a potential explanation is seen in the Lyα emission and galaxy density in the center of the cluster. The thermal gas and galaxies are asymmetrically distributed in the cluster, with a higher density toward the west than the east. It is possible that this density inhomogeneity, in a dynamically active and young protocluster, leads to more disturbed jet advance toward the west, while the eastern jet remains relatively unperturbed until it reaches the terminal jet shock (hot spot). The perturbed nature of the western jet is supported by the bright Lyα knot at the jet deflection point, discussed above.

We note the very steep spectra for the diffuse emitting regions of the Spiderweb, such as in the eastern lobe and the end of the western jet, where $\alpha < -2$ (see Figures 4 and 6). This may, in part, be due to increasing IC energy losses off the CMB for the relativistic electrons. Indeed, this phenomenon

has been invoked to explain the correlation between redshift and ultra-steep-spectrum radio galaxies (for a review, see Miley & de Breuck 2008). The VLA snapshot survey of Pentericci et al. (2000) shows evidence that the majority of $z > 2$ powerful radio galaxies have lobe regions with very steep spectra ($\alpha < -2$ between 5 and 8 GHz), although the snapshot sensitivity of the pre-upgraded VLA was inadequate to properly image these regions in detail.

A general question is, given the rapid rise with redshift of the energy density in the CMB, at what redshift will cooling of the relativistic electrons be dominated by IC emission over synchrotron radiation? The calculation is straightforward, since the ratio of radio synchrotron to X-ray luminosity is given simply by $L_r/L_x = U_B/U_{\mathrm{CMB}}$ (Carilli & Taylor 2002; Schwartz 2002). The magnetic energy density in a radio source is $U_B \sim 1 \times 10^{-10}(B/50\ \mu\mathrm{G})^2$ erg cm^{-3}, while the CMB energy density is $U_{\mathrm{CMB}} = 4.2 \times 10^{-13} \times (1+z)^4$ erg cm^{-3}. Hence, $L_x > L_r$ at $(1+z) > 3.9 \times (B/50\ \mu\mathrm{G})^{1/2}$. For typical radio jet magnetic fields of 50 μG, IC dominates over radio synchrotron losses at $z > 2.9$. A recent analysis of 11 radio galaxies from $z = 1.3$ to 4.3 shows that, for the diffuse emission, the X-ray and radio data are consistent with both IC scattering of the CMB and equipartition magnetic fields (Hodges-Kluck et al. 2021).

6. Summary

Using the observed IC and radio synchrotron radiation, we derive typical magnetic field strengths in the jets of the Spiderweb ~ 50–70 μG, in regions of the source beyond 20 kpc from the core. These are regionally averaged values, derived over areas of significant radio structure, and hence represent a brightness weighted mean, that is, weighted toward knots and hot spots, corresponding to regions of particle acceleration due to shocks or regions of high compression.

The IC fields are a factor of two lower than those derived assuming a minimum energy ($\sim$equipartition) configuration for the synchrotron-emitting relativistic particles and fields. The implied nonthermal pressure (sum of relativistic particles and fields), implied by the combination of IC X-rays and radio synchrotron radiation, is $\sim 9 \times 10^{-10}$ dynes cm^{-2}. This nonthermal pressure is a factor of three higher than the pressure derived by assuming minimum energy conditions, and the pressure is dominated by relativistic particles. Comparing the typical nonthermal pressure in the radio source with the thermal pressure in the ambient cluster gas derived from Lyα emission and from possible diffuse thermal X-ray emission implies a factor of 15 higher pressures in the brighter radio-emitting regions than in the ambient thermal gas. Assuming ram pressure confinement of the radio source by a hypothesized hot, diffuse cluster gas implies an advance speed of ~ 2400 km s^{-1} and a radio source lifetime of $\sim 3 \times 10^7$ yr.

We see two regions where there is a clear spatial correlation between radio structures and the Lyα-emitting gas. One region is the brightest Lyα knot in the western jet coincident with the position where the radio jet deflects toward the southwest. This deflection suggests a strong shock due to the impact of the radio jet on an ambient density enhancement. We will discuss this region in detail in our polarization analysis of the radio emission (C. Anderson et al. 2021, in preparation).

The second spatial association of the Lyα and radio emission is seen in the tail of the eastern lobe, where the radio lobe appears evacuated of Lyα emission, while the line emission

outer edge (away from the AGN) aligns closely with the inner edge of the radio lobe. This anticorrelated morphology is reminiscent of cavities in X-ray clusters due to expanding radio sources (McNamara et al. 2005). A calculation of the minimum pressure in the nonthermal gas in the faintest radio-emitting regions, based on 3 GHz surface brightness, and assuming a spectral flattening between 0.5 and 1.0 GHz, leads to approximate pressure equilibrium between the minimum nonthermal pressures and the ambient thermal cluster gas. In the context of the standard model for powerful radio galaxies, in which the lobes represent the older, more relaxed populations of relativistic particles and fields left behind by the expanding radio source, it seems physically plausible that a minimum energy configuration for fields and particles would be more likely in the relaxed lobes. Spatially resolving observations at low frequency would help to test this hypothesis.

We show that the Spiderweb radio source is a high-redshift example of a "hybrid morphology" radio source, with the western jet having the morphology in total intensity and spectral index of an FR I class radio galaxy (edge-darkened) and the eastern region having the morphology of an FR II class radio galaxy (edge-brightened) (Gopal-Krishna 2000). The origin of such HyMoRS remains an area of active research. In the case of the Spiderweb, a clue to the origin may be seen in the asymmetric gas environment, for which the Lyα emission is predominantly west of the nucleus, potentially leading to higher disruption of the advancing radio jet.

ORCID iDs

Christopher L. Carilli ⓘ https://orcid.org/0000-0001-6647-3861
Paolo Tozzi ⓘ https://orcid.org/0000-0003-3096-9966
Tracy Clarke ⓘ https://orcid.org/0000-0001-6812-7938
L. Pentericci ⓘ https://orcid.org/0000-0001-8940-6768
Tony Mroczkowski ⓘ https://orcid.org/0000-0003-3816-5372
S. Borgani ⓘ https://orcid.org/0000-0001-6151-6439
Colin Norman ⓘ https://orcid.org/0000-0002-5222-5717

References

Blandford, R. D., & Payne, D. G. 1982, MNRAS, 199, 883
Briggs, D., Schwab, F., & Sramek, R. 1999, in in Synthesis Imaging in Radio Astronomy II, ed. G. B. Taylor, C. L. Carilli, & R. A. Perley, 180 (San Francisco: ASP), 127
Burbidge, G. 1956, ApJ, 124, 416
Carilli, C. L. 1989, PhD Thesis, MIT
Carilli, C. L., Harris, D. E., Pentericci, L., et al. 2002, ApJ, 567, 781
Carilli, C. L., Miley, G., Röttgering, H. J. A., et al. 2001, in Gas and Galaxy Evolution, ed. J. E. Hibbard, M. Rupen, & J. H. van Gorkum (San Francisco: ASP), 101
Carilli, C. L., & Taylor, G. B. 2002, ARA&A, 40, 319
Cheung, C. C., Stawarz, L., Siemiginowska, A., et al. 2012, ApJL, 756, L20
Clarke, T. E., Kassim, N. E., Brisken, W., et al. 2016, Proc. SPIE, 9906, 99065B
Cotton, W. D. 2008, PASP, 120, 439
Dannerbauer, H., Kurk, J. D., De Breuck, C., et al. 2014, A&A, 570, 55
de Gasperin, F. 2017, MNRAS, 467, 2234
Emonts, B., Lehnert, M., Villar-Martin, M., et al. 2016, Sci, 354, 1128
Fabian, A. C. 2012, ARA&A, 50, 455
Fanaroff, B., & Riley, J. 1974, MNRAS, 167, 31
Gaibler, V., Khochfar, S., Krause, M., & Silk, J. 2012, MNRAS, 425, 438
Gawronski, M., Marecki, A., Kunert-Bajraszewska, M., & Kus, A. 2006, A&A, 447, 63
Gopal-Krishna, P. W. 2000, A&A, 363, 507
Gullberg, B., Lehnert, M., de Breuck, C., et al. 2016, A&A, 591, A73
Harris, D. E., & Grindlay, J. E. 1979, MNRAS, 188, 25
Harwood, J. J., Vernstrom, T., & Stroe, A. 2020, MNRAS, 491, 803
Hodges-Kluck, E., Gallo, E., Ghisellini, G., et al. 2021, MNRAS, 505, 1543
Ighina, L., Caccianiga, A., Moretti, et al. 2019, MNRAS, 489, 2732
Jin, S., Dannerbauer, H., Emonts, B., et al. 2021, A&A, 652, 11
Kapinska, A., Terentex, I., Wong, O. I., et al. 2017, AJ, 154, 253
Kurk, J., Röttgering, H. J. A., Pentericci, L., et al. 2000, ApJL, 351, L1
Longair, M. 2011, High Energy Astrophysics (Cambridge, UK: Cambridge Univ. Press)
Marshall, H. L., Gelbord, J. M., Worrall, D. M., et al. 2018, ApJ, 856, 66
McCarthy, P. 1993, ARA&A, 31, 639
McNamara, B. R., Nulsen, P. E. J., Wise, M. W., et al. 2005, Sci, 433, 45
Miley, G. 1980, ARA&A, 18, 165
Miley, G., & de Breuck, C. 2008, A&ARv, 15, 67
Miley, G., Overzier, R., Zim, A., et al. 2006, ApJL, 650, L29
Pentericci, L., Roettgering, H. J. A., Miley, G. K., Carilli, C. L., & McCarthy, P. 1997, A&A, 326, 580
Pentericci, L., Rottgering, H. J. A., Miley, G. K., et al. 1999, ApJ, 504, 139
Pentericci, L., van Reeven, W., Carilli, C. L., et al. 2000, A&AS, 361, 25
Readhead, A. 2021, Lecture Notes in Radiative Processes, Caltech, AY121
Scharf, C., Smail, I., Ivison, R., et al. 2003, ApJ, 596, 105
Schwartz, D. A. 2002, ApJL, 571, L71
Schwartz, D. A., Siemiginowska, A., Snios, B., et al. 2019, ApJ, 904, 57
Seymour, N., Altieri, B., De Breuck, C., et al. 2012, ApJ, 755, 146
Simionescu, A., Stawarz, L., Ichinohe, Y., et al. 2016, ApJL, 816, L15
Snios, B., Nulsen, P. E., Wise, M. W., et al. 2018, ApJ, 855, 71
Snios, B., Schwartz, D. A., Siemiginowska, A., et al. 2021, ApJ, 914, 130
Tavecchio, F., Maraschi, L., Sambruna, R. M., & Urry, C. M. 2000, ApJL, 544, L23
Tozzi, P., Pentericci, L., Gilli, R., et al. 2021, A&A, in press
van Moorsel, G., Kemball, A., & Greisen, E. 1996, in Astronomical Data Analysis Software and Systems V, ASP Conf. Ser. 101 (San Francisco, CA: ASP), 37
Worrall, D. M., Birkinshaw, M., Marshall, H. L., et al. 2020, MNRAS, 497, 988